Supplement of

A multi-model analysis of the transatlantic dust transport, deposition, and optical properties in the AeroCom Phase III

Jianyu Zheng et al.

Correspondence to: Jianyu Zheng (jzheng3@umbc.edu)

Descriptions of observational data

S1 Satellite observations

To evaluate the dust modeling results on a large scale, satellite observations are the optimal option to serve as the observational constraints in terms of spatial variations of dust properties.

S1.1 MODIS mid-visible DOD

As traditional AOD retrievals in the shortwave spectrum contain contributions from both dust and non-dust aerosols, MODIS mid-visible (at 0.55μm) DOD is derived from AOD retrievals with the Dark Target (DT) over oceans and Deep Blue (DB) over land using different assumptions about distinct size and absorption spectra. Over oceans, MODIS DT AOD and fine-mode fraction (f) measurements have been used to empirically separate dust (du) from that of combustion aerosol (co) and marine aerosol (ma) in a self-consistent way (Kaufman et al., 2005; Yu et al., 2015a; Yu et al., 2009; Yu et al., 2020). Given that $\tau = \tau_{ma} + \tau_{du} + \tau_{co}$ and $f = [f_{ma}\tau_{ma} + f_{du}\tau_{du} + f_{co}\tau_{co}]/\tau$, DOD ($\tau_{du}$) is derived from the MODIS Collection 6.1 data using wind-speed-dependent τ_{ma} and representative values for f_{ma}, f_{du}, f_{co} (determined from MODIS FMF retrievals in regions predominated by marine, dust, and combustion aerosol, respectively) (Yu et al., 2020). Over land, DOD is extracted from the MODIS DB AOD based on (1) the cofunction of the continuous Angstrom exponent values derived by Anderson et al. (2005), (2) single scattering albedo ω at 412 nm less than 1, and (3) a positive difference of ω between 412 and 670 nm ($\omega_{670} - \omega_{412} > 0$) (Ginoux et al., 2012; Pu and Ginoux, 2018).

S1.2 CALIOP mid-visible DOD and dust extinction profile

The dust vertical distribution fundamentally affects dust transport patterns and atmospheric lifetime, as dust at different altitudes experiences varying wind and hydrometeor patterns, determining surface deposition rates. Therefore, in this study, we evaluate the model-simulated dust extinction coefficients by comparing them with those from CALIOP, which are estimated based on the particulate depolarization ratio (PDR) at 532 nm, as most non-dust aerosols are nearly spherical particles with a small PDR (0.02–0.07), while dust is mostly irregularly non-spherical and thus has a higher PDR (0.2–0.3). In this study, we use the CALIOP 5° × 2° monthly DOD at 532 nm and dust vertical distribution from Song et al. (2021), which was derived based on the PDR method developed in Yu et al. (2015a).

S1.3 IASI AOD at 10 μm

The Infrared Atmospheric Sounding Interferometer (IASI) on board the Metop satellites provides unique capabilities for retrieving DOD and dust layer altitude using thermal infrared (TIR) window spectrum (8-13 μm), which are particularly sensitive to coarse-mode dust particles due to their distinct spectral signatures. There are multiple research products of DOD at 10 μm retrieved using IASI that are developed by different research groups. In this study, we use the DOD product developed by the research group at Laboratoire de Météorologie Dynamique (LMD), which is based on a two-step look-up table method (Capelle et al., 2018). The DOD at 550 nm is also provided by IASI-LMD, which is converted from the retrieved DOD at 10 μm using conversion factors based on their inherent assumptions of dust refractive index and particle size distribution (Capelle et al., 2018).

S1.4 MISR mid-visible DOD

The Multi-angle Imaging SpectroRadiometer (MISR) on NASA's Terra satellite provides unique multi-angle observations that enable discrimination of aerosol particle properties, including particle non-sphericity, which is a key characteristic for distinguishing mineral dust (predominantly nonspherical particles) from other aerosol types. In this study, we use MISR Version 23 (V23) nonspherical AOD at 0.558 μm to represent DOD, following the methodology of Kahn and Gaitley (2015) and Garay et al. (2020). The nonspherical AOD from MISR over land, especially over bright desert surfaces, may be underestimated (Kahn et al., 2010; Xi et al., 2025). The MISR data are originally provided at 0.5° × 0.5° spatial resolution and are re-gridded to 1° × 1° using area-weighted averaging to maintain consistency with other satellite products and model outputs in this study.

S1.5 POLDER mid-visible DOD and mass loading

Satellite retrieval for aerosol mass loading is challenging. Recently, Li et al. (2022) retrieved aerosol component concentrations by applying the GRASP/Component algorithm to the full archive of POLDER-3, a satellite polarimeter onboard PARASOL that measured multi-angular, multi-spectral, and polarized radiances at up to 16 viewing angles from March 2005 to October 2013. The approach directly retrieves volume fractions of aerosol components from these measurements without intermediate retrieval of bulk optical properties, using the Maxwell-Garnett mixing rule with fixed component refractive indices. Validation of the retrieved optical properties against AERONET shows good agreement, and CNAI spatial patterns are compared with MERRA-2 dust column concentrations, revealing generally consistent distributions (Li et al., 2022) .

In this study, we use coarse-mode AOD at 565 nm and the coarse-mode insoluble and iron mass concentration to represent mid-visible DOD and coarse dust mass loading over trans-Atlantic regions. It should be noted that this proxy would have potential misattributions of coarse-mode dust from non-dust coarse aerosol components. Therefore, we leverage the coarse-mode insoluble and iron volume fraction to derive the insoluble and iron coarse-mode AOD at 565 nm (denoted as COD_{dust}) to investigate the appropriateness of using coarse-mode AOD as a proxy for dust over trans-Atlantic regions, which is discussed in Section 3.2.1.

S1.6 MODIS-TIR dust product

As the dust vertical distribution shares the same order of sensitivity as DOD in TIR observations, hyperspectral sensors retrieve both DOD and dust layer, leaving limited room for retrieving dust microphysical properties. To overcome such challenges, building upon Zheng et al. (2022), Zheng et al. (2023) combine MODIS TIR observations with CALIOP dust vertical profiles to simultaneously retrieve coarse-mode DOD and effective diameter over global oceans. Recently, Zheng et al. (2026) further improved the algorithm by addressing the challenges of variable surface emissivity over land and increased the retrieval coverage with 10-km spatial resolution, with strong validation against AERONET and in situ measurements from field campaigns worldwide. The resulting dataset from Zheng et al. (2026) provides valuable constraints on dust size distribution in the broader coarse mode domain (1-100 μm) that are not sensitive enough to be retrieved in visible-near-infrared spectra (Ryder et al., 2019; Zheng et al., 2024). The coarse dust size is also important for accurately calculating MEE, which is key for estimating dust mass concentration for constraining uncertainties from model simulations.

S1.7 Satellite-based estimates of trans-Atlantic dust deposition

Yu et al. (2019) developed a satellite-based methodology to estimate dust deposition fluxes along the trans-Atlantic transit corridor. The approach derives the 3-D dust mass concentration fields by distributing monthly mid-visible DOD from MODIS, MISR, and IASI in the vertical using CALIOP dust extinction profiles and then converting dust extinction to mass concentration using MEE values of 0.37–0.6 $m^2 g^{-1}$. Horizontal dust mass fluxes entering and leaving the 5° × 2° cell are then calculated by combining the mass concentrations with zonal and meridional winds from the MERRA-2 reanalysis. Dust deposition flux into the ocean is estimated as the residual from the divergence of vertically integrated horizontal dust mass fluxes under the assumptions that there are no dust sources over the ocean and African dust is not transported vertically across the altitude of 10 km. This flux-divergence approach yields estimates of total (dry plus wet) deposition over open ocean areas where no surface dust emission occurs. The dust loss frequency, defined as the ratio of deposition flux to column dust mass loading (day^{-1}), is simultaneously derived to characterize the efficiency of atmospheric dust removal independent of the absolute dust burden. These satellite-based deposition flux and loss frequency estimates provide a unique observational benchmark over the open Atlantic, where in-situ deposition measurements are sparse.

S1.8 Precipitation rate from Global Precipitation Climatology Project

Precipitation is the main driver of wet scavenging—the process that removes dust particles from the atmosphere via rainout (in-cloud) and washout (below-cloud) processes. For mineral dust, wet deposition often accounts for 20–70 % of total removal, depending on region and season (higher fractions in long-range transport regions) (Audoux et al., 2022; Zhao et al., 2022); biases in modeled precipitation can propagate directly into errors in dust removal processes. To evaluate the fidelity of precipitation fields in the AeroCom P3 models, we use the 2.5° × 2.5° monthly precipitation rates in 2010 from the Global Precipitation Climatology Project (GPCP) Version 2.3 monthly analysis (Adler et al., 2018).

S2 In-situ and ground-based observational data

S2.1 In-situ dust deposition climatology

In-situ measurements of dust deposition are often acquired from surface collectors, oceanic sediment traps, and atmospheric sampling of dust proxies (Anderson et al., 2016). In this study, we assemble a compilation of 42 in-situ deposition sites over trans-Atlantic regions drawn primarily from the widely referenced data set of Albani et al. (2014) and supplemented with more recent Trans-Atlantic sediment trap records (Friese et al., 2017; Korte et al., 2017; and references therein). A caveat is that 25 of the 42 sites were sampled before the satellite era (i.e., before 2000). In addition, the use of lithogenic proxies to infer dust fluxes introduces additional uncertainty that varies by methodology and site. Given this temporal mismatch and the large interannual variability inherent to dust emissions, the comparisons with in-situ dust deposition climatology presented here should be interpreted as cross-checks among independent methods rather than rigorous point-by-point validations. Details of each in-situ deposition site are presented in Table S3.

S2.2 Near-surface dust mass concentration

Long-term ground-based measurements of surface dust mass concentrations at Ragged Point, Barbados (13°6′N, 59°37′W; initiated in the mid-1960s) and Miami (25°45′N, 80°15′W; began in

July 1974) constitute one of the most valuable in situ multi-decadal records for understanding trans-Atlantic African dust transport (Zuidema et al., 2019). At the two stations, dust samples are collected on Whatman-41 filters at flow rates of approximately 1 $m^3\ min^{-1}$, with local source contamination minimized by restricting sampling to periods when winds arrive from open ocean sectors exceeding 1 $m\ s^{-1}$ (Morton et al., 2013). In this study, we use the monthly data in 2010 to evaluate the AeroCom P3 models.

S2.3 AERONET retrievals of dust component - DOD and dust mass loading

The Aerosol Robotic Network (AERONET) is a global network of ground-based sun photometers that provides high-quality, calibrated measurements of AOD at multiple wavelengths (Holben et al., 1998). The Spectral Deconvolution Algorithm (SDA; O'Neill et al., 2003) separates the total AOD into fine-mode and coarse-mode contributions based on the spectral curvature of the measured AOD spectrum. Coarse-mode AOD from the SDA serves as a reliable proxy for DOD at dust-dominated sites, as mineral dust dominates the coarse aerosol fraction in such regions. In this study, we convert Level 2.0 (quality-assured) SDA coarse-mode AOD at 550 nm (converted from 500 nm using Angstrom Exponents of 440-870 nm) from 18 AERONET stations within the studied region. Furthermore, to evaluate the AOD annual variation, we selected 5 sites over trans-Atlantic dust transport corridor that are predominantly influenced by Saharan dust and have data coverage > 9 months in 2010: Tamanrasset (22.79°N, 5.53°E) and Banizoumbou (13.54°N, 2.66°E) in the NAF source region, Dakar (14.39°N, 16.96°W) at the West African coast, Capo Verde (16.73°N, 22.94°W) in the eastern Atlantic, and Ragged Point (13.16°N, 59.43°W) in the Caribbean. These five sites span the full trans-Atlantic pathway and provide an independent validation of DOD from source to receptor regions.

In addition to DOD, we also use the AERONET-based aerosol component retrieval product from Zhang et al. (2024) to evaluate dust mass loading. This product applies the GRASP component inversion approach (Li et al., 2019) to AERONET Level 1.5 directional sky radiances and spectral AOD, directly retrieving volume fractions of aerosol components with known complex refractive indices using the Maxwell–Garnett mixing rule. Two non-absorbing insoluble components represent dust: the coarse-mode (CNAI, mainly mineral dust) and fine-mode (FNAI, fine dust and aged carbonaceous aerosols) fractions, whose summed column mass concentrations estimate total non-absorbing dust loading. While the retrieved optical properties agree well with AERONET Level 2.0 standard products, the mass loading lacks independent in-situ or aircraft-based compositional validation, as global whole-column observations of aerosol composition remain scarce. Key uncertainties include higher retrieval error at low AOD ($AOD\_440nm \leq 0.2$) and potential misattribution between brown carbon and iron oxides in dust.

S3 DustCOMM climatology of the dust inverted model

DustCOMM (Dust Constraints from joint Observational-Modelling-experiMental analysis) integrates observational constraints (including dust size distribution, aspherical dust shape, and satellite-modeling-derived DOD) with global model simulations to yield improved estimates of atmospheric dust properties (Adebiyi et al., 2020; Kok et al., 2021). In this study, we compare AeroCom P3 models with DustCOMM for dust properties across particle geometric diameters of 10 μm (PM10), and 20 μm (PM20). However, we should note that DustCOMM DOD is seasonally averaged within 2004-2008. Such temporal differences with AeroCom P3 and satellite observations from 2010 may have potential differences in meteorological conditions and DOD.

S4 MERRA-2 and CAMS reanalysis products

The Modern-Era Retrospective Analysis for Research and Applications, Version 2 (MERRA-2; Gelaro et al., 2017) and the Copernicus Atmosphere Monitoring Service (CAMS) reanalysis (Inness et al., 2019) provide global, gridded aerosol fields produced by assimilating satellite-retrieved total AOD into their underlying atmospheric models. In MERRA-2, bias-corrected AOD retrievals from MODIS (Terra and Aqua), MISR, and AVHRR, together with AERONET measurements, are assimilated into the Goddard Earth Observing System (GEOS) model coupled with the GOCART aerosol module, yielding three-dimensional dust mass mixing ratios across five size bins. In the CAMS reanalysis, total AODs from MODIS and the Polar MultiSensor Aerosol Optical Properties (PMAp) are assimilated into the ECMWF Integrated Forecasting System with the bin-resolved aerosol scheme of Morcrette et al. (2009). From both reanalyses, in this study, we obtain the monthly mean DOD at 550 nm and column-integrated dust mass loading in 2010 for comparison with the AeroCom P3 simulations across the trans-Atlantic corridor. We emphasize, however, that although total AOD is nudged toward satellite observations in both reanalyses, dust-specific quantities are not directly constrained. Instead, they are inferred from the assimilated total AOD through each system's internal partitioning among aerosol species, which depends on emission inventories, optical assumptions, and transport and removal processes in the host model. Consequently, MERRA-2 and CAMS dust products should be regarded as observation-informed model estimates rather than direct observations, and inter-product differences provide an additional measure of structural uncertainty in reanalysis-based dust fields.

S5 Dust mass loading estimation from POLDER and MODIS-TIR

To have independent references of dust mass from observations, we first approximate the GRASP-retrieved AERONET non-absorbing insoluble mass concentration as mainly contributed by dust. For POLDER, we use the insoluble and iron components to represent the dust mass concentration. As the POLDER product reports aerosol volume concentrations, the mass loading for dust is further derived as

$$Mass_{dust} = V_{insoluble} \cdot \rho_{insoluble} + V_{iron} \cdot \rho_{iron}$$

where $\rho_{insoluble}$ and ρ_{iron} represents the assumed density of insoluble dust (2.65 g cm^{-3}) and iron oxide (4.8 g cm^{-3}). The corresponding AOD contributed by insoluble and iron components or DOD is derived as

$$DOD_{dust} = AOD_{565nm} \cdot \frac{V_{insoluble} + V_{iron}}{V_{all}}$$

where $V_{insoluble}$, V_{iron}, and V_{all} represent the volume concentration of insoluble, iron and all aerosol components. The column-integrated MEE is further obtained as $DOD_{dust}/Mass_{dust}$.

In addition, the MODIS-TIR product from Zheng et al. (2026) provides simultaneous retrieval of DOD at 10 μm and coarse mode D_{eff} spanning 1 to 14 μm, which can be used to calculate the column-integrated effective MEE for dust (D > 1 μm) as

$$MEE_{dust,\lambda} = \frac{3}{2} \cdot \frac{Q_{ext}(\lambda, m, D_{eff})}{\rho \cdot D_{eff}}$$

where Q_{ext} represents bulk extinction coefficient, ρ, λ and m represent the dust density (also assumed to be 2.65 g cm^{-3}), wavelength, complex refractive index used in the retrieval, respectively. Deff represents the retrieved effective diameter of the coarse-mode PSD. Note that we approximate the converted AOD from the MODIS-TIR as DOD in this study. Therefore, to be consistent, we also use the derived coarse mass as a proxy for dust mass loading, which can be obtained as

$$Mass_{dust} = \frac{DOD_{10\mu m}}{MEE_{dust,10\mu m}} = \frac{DOD_{550nm,converted}}{MEE_{dust,550nm}}$$

Note that the two satellite products adopt distinct approaches to estimate dust mass, each carrying specific assumptions about aerosol composition, shape, size, and density as mentioned above, which introduce systematic uncertainties. These differences must be kept in mind when comparing satellite-derived mass loading with reanalysis-based products and AeroCom model outputs.

Tables and Figures

Table S1: Domain average of available variables from individual models for inter-comparisons.

Size Group	Model	NAF Emission Rate (mg/m²/d)	Mass loading (g/m²)	DOD 550nm	Surface concentration (µg/m³)	Total deposition rate (mg/m²/d)	Precipitation rate (mm/d)
Group 1	CAM5-ATRAS	240.0	0.1962	0.0770		51.5284	2.0141
	EC-Earth3-AerChem	69.6	0.0831	0.0900	30.5100	14.2126	2.5733
	ECHAM-HAM	117.5	0.1463	0.1119		22.6391	
	ECHAM-SALSA	153.9163	0.1839	0.1315		15.4558	1.3183
	INCA	157.3788	0.1860	0.1520	71.1437	23.2289	2.6956
	NorESM2	94.9010	0.0437	0.0706		21.5488	2.2442
	TM5	89.4478	0.0993	0.1016	34.8963	19.1811	3.2485
Group 2	BCC-CUACE	271.7153	0.1196		56.2516	62.2151	1.9661
	ECMWF-CY45	173.8890	0.1077	0.0896	39.7131	39.8089	
	GEOS	167.8725	0.2170	0.1303	98.7166	35.2868	2.9520
	GFDL-AM4	113.4867	0.1075	0.0812		25.2787	2.7407
	GISS-MATRIX	82.3232	0.1490			14.5623	1.9381
	GISS-OMA	172.0775	0.1935	0.0960		34.8191	1.9811
	OsloCTM3	198.8061	0.1907	0.1218		42.5957	
	SPRINTARS	216.9933	0.0987	0.0695		48.0491	2.5717
Group 3	ECMWF-CY46	585.7576	0.2347	0.1083	78.4138	139.5487	
	INCA-4DU	1689.230	0.4220	0.1509	223.5380	396.5861	2.7100

Table S2: Regional domain average of mean, median and diversity of available variables from Group 1 and 2 models.

Statistics	Region	Emission Rate (mg/m²/d)	Mass loading (g/m²)	DOD 550nm	Surface concentration (µg/m³)	Total deposition rate (mg/m²/d)	Precipitation rate (mm/d)
Mean	NAF	154.66	0.4	0.27	185.1	95.53	0.67
	GOG		0.05	0.05	10.06	11.47	2.4
	EAO		0.09	0.07	20.8	13.46	2.83
	CAR		0.02	0.02	4.86	4.99	3.52
Median	NAF	157.38	0.35	0.26	164.83	80.26	0.65
	GOG		0.05	0.05	8.43	10.38	2.15
	EAO		0.1	0.07	19.27	12.13	2.91
	CAR		0.15	0.02	3.3	4.71	3.57

Diversity	NAF	39%	41%	30%	48%	64%	38%
	GOG		53%	52%	62%	55%	44%
	EAO		42%	37%	52%	40%	26%
	CAR		52%	46%	77%	47%	20%

Table S3: The geolocation, sampling period, and dust deposition climatology from the 42 selected in-situ measurements within the trans-Atlantic region.

location	Latitude	Longitude	Sampling period	Deposition ($mg/m^2/year$)	original reference
Eilat, Israel	29.52	34.92	2003-2004	5819.14	Chase et al. 2006
Dead Sea, Israel	31.5	35.3	1997-1999	44500.00	Singer et al. 2003
Lake Kinneret, Israel	32.7	35.5	1992-1997	287400.00	Ganor et al. 2003
Negev Desert, Israel	34.8	30.8	1997-1999	45000.00	Goossens 2000
Crete	35.2	24.8	1988-1992	21270.86	Nihlén et al. 1995
Algeciras, S Spain	36.3	-5.4	1982-1983	22800.00	Usero and Gracia 1986
22N25W	21.93	-25.23	1986-1987	6700	Kremling and Streu 1993; Jickells et al. 1996
CB2-2	21.15	-20.69	1989-1990	20480	Ratmeyer et al. 1999; Wefer and Fischer 1993
CB2-1	21.15	-20.68	1989-1990	19700	Fischer et al. 1996; Wefer and Fischer 1993
BOFS-1	19	-20.17	1990-1991	21550	Bory and Newton 2000
Eumeli mesotrophic	18.5	-21.08	1991	18740	Bory and Newton 2000
CV 1 upper	11.48	-21.02	1992-1993	22620	Ratmeyer et al. 1999
CB1-1	20.92	-19.75	1988-1989	21920	Fischer et al. 1996; Wefer and Fischer 1993
CB1-2	20.92	-19.74	1989-1990	27200	Jickells et al. 1996; Wefer and Fischer 1993
CB1-3	20.92	-19.74	1990-1991	11390	Ratmeyer et al. 1999; Wefer and Fischer 1993
CI 1 upper	29.11	-15.45	1991-1992	4150	Ratmeyer et al. 1999; Wefer and Fischer 1993
GBN3 upper	1.79	-11.13	1989-1990	4300	Wefer and Fischer 1993
GBZ4	-2.18	-9.9	1989-1990	1200	Wefer and Fischer 1993
L1-93	33.15	-21.98	1993-1994	1170	Kuss and Kremling 1999
L1-93	33.15	-21.98	1993-1994	2340	Kuss and Kremling 1999
SARGASSO	32.08	-64.25	1981-1991	1900	Jickells et al. 1998
Eumeli oligotrophic	21.05	-31.17	1991-1992	3730	Bory and Newton 2000
25N23W	24.55	-22.83	1990-1991	5210	Jickells et al. 1996
28N22W	28	-21.98	1990-1991	2400	Jickells et al. 1996
34N21W	33.82	-21.02	1989-1990	4750	Honjo and Manganini 1993
Miami	25.75	-80.25	1982-1983	1620	Prospero et al. 1987
Mallorca	40	-7.0	1982-2003	13500	Fiol et al. 2005
North Libya	32	13	2000-2001	129000	O'Hara et al. 2006
Zillah - Central Libya	28.5	16.25	2000-2001	276000	O'Hara et al. 2006
Birak - South Libya	27.25	14	2000-2001	82000	O'Hara et al. 2006
Niger	13	2	1985-1989	200000	Drees et al. 1993
Northern Nigeria	12.1	8.5	1976-1979	159000	McTainsh and Walker 1982
Northern Nigeria	12	8	1984-1985	85000	Moberg et al. 1991
Ghana	7.5	-34.0	2002, 2005	22000	Resch et al. 2008
Cote d'Ivoire	7.3	5.9	1990-1991	8000	Stoorvogel et al. 1997
Cbi upper	20.75	-18.75	2013-2014	28470	Friese et al. (2017)

CB	21.26	-20.84	2013	16425	Friese et al. (2017)
DustTraffic M1 Upper	12	-23	2013	17400	Korte et al. (2017)
DustTraffic M2 Upper	13.81	-37.82	2013	3900	Korte et al. (2017)
DustTraffic M4 Upper	12.06	-49.19	2013	8700	Korte et al. (2017)
Majorca	39.25	3.05	2013	5800	Vincent et al. (2016)
Lampedusa	35.51	12.51	2012	7400	Vincent et al. (2016)

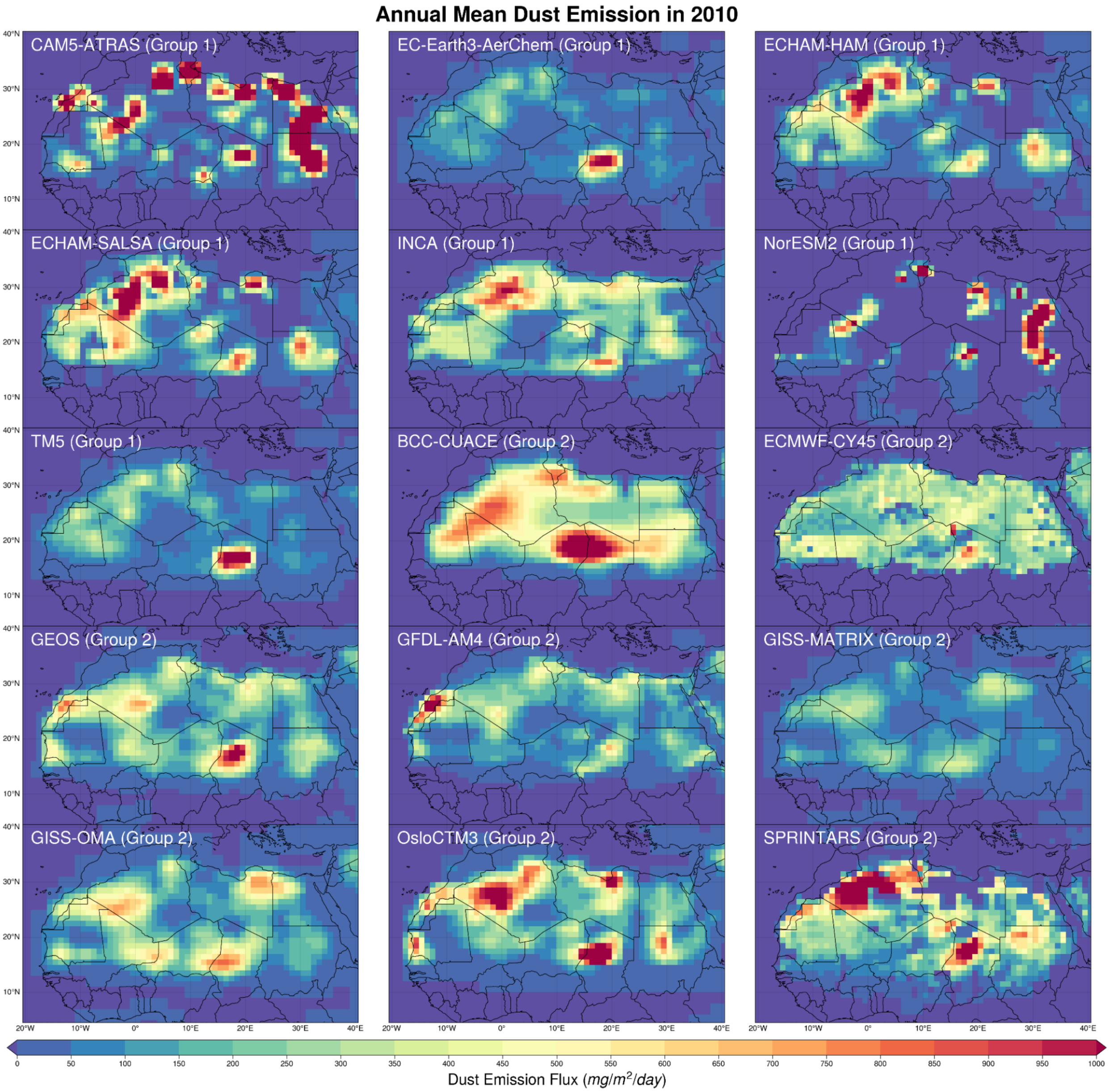

Figure S1: The annual mean dust emission fluxes (mg m^{-2} d^{-1}) over North Africa simulated by the AeroCom Phase III models.

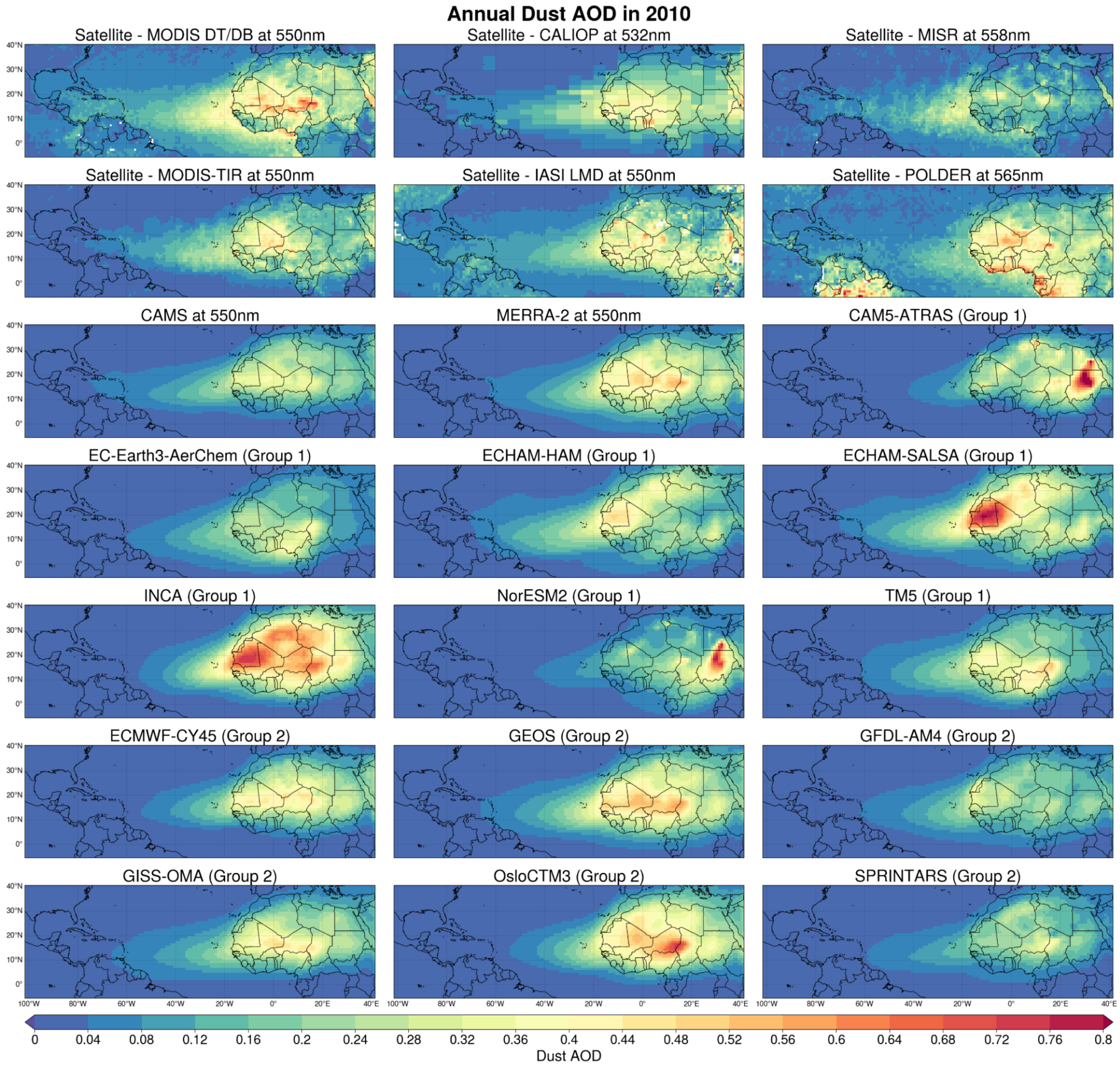

Figure S2: Annual mid-visible DOD from the satellite observations (MODIS, CALIOP, MISR, POLDER, MODIS-TIR, IASI-LMD), reanalysis products (CAMS and MEERA-2), and 13 AeroCom Phase III models.

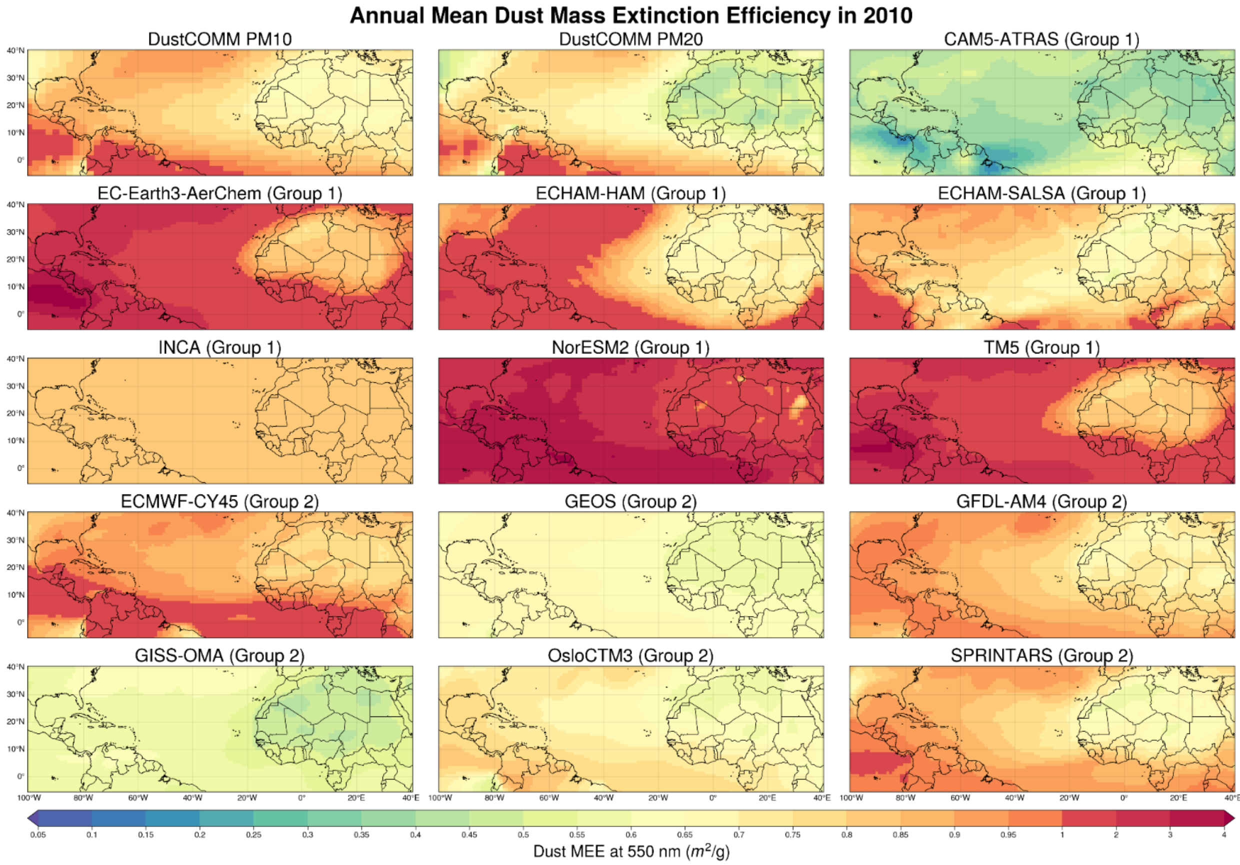

Figure S3: The mass extinction efficiency (m^2 g^{-1}) at 550 nm from DustCOMM and 13 AeroCom Phase III models.

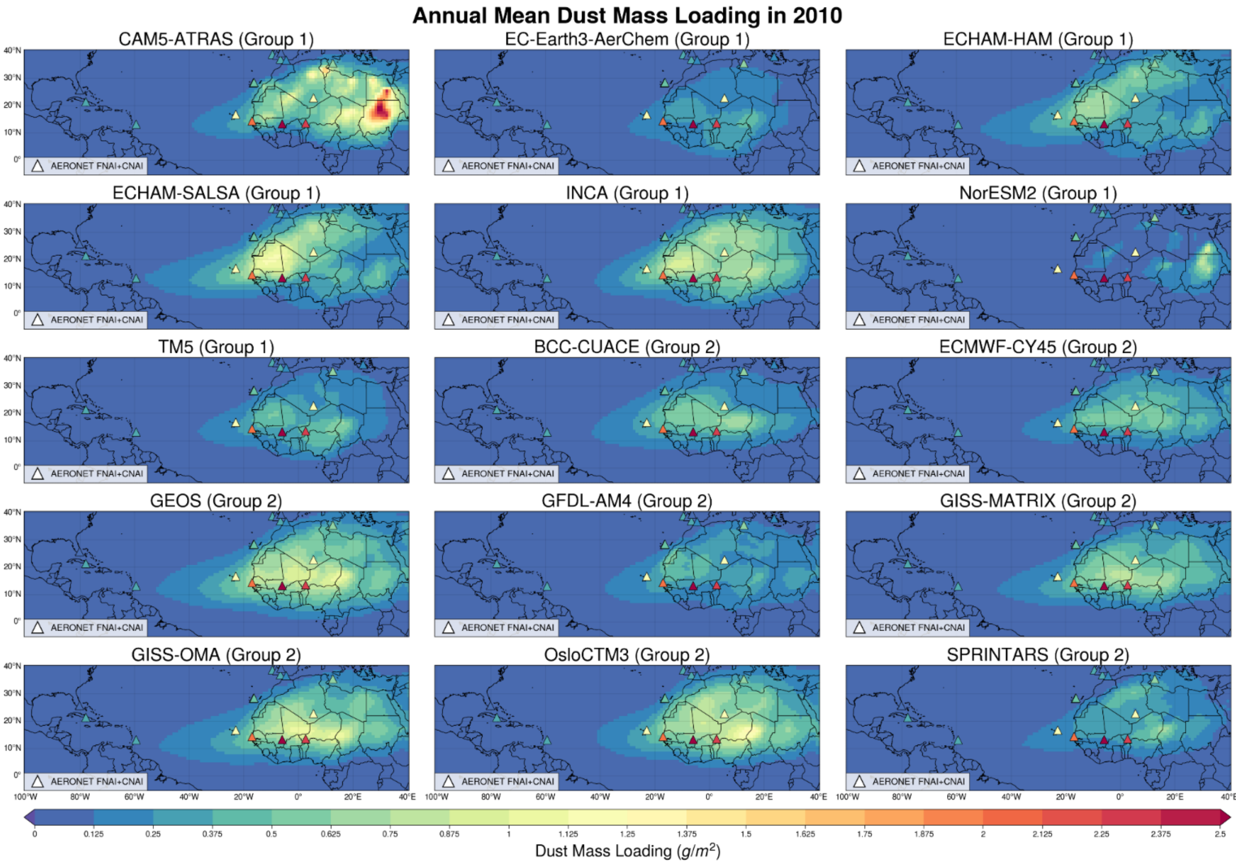

Figure S4: The dust mass loading (g m^{-2}) from 15 AeroCom Phase III models. The color triangles represent the AERONET retrievals of CNAI mass loading.

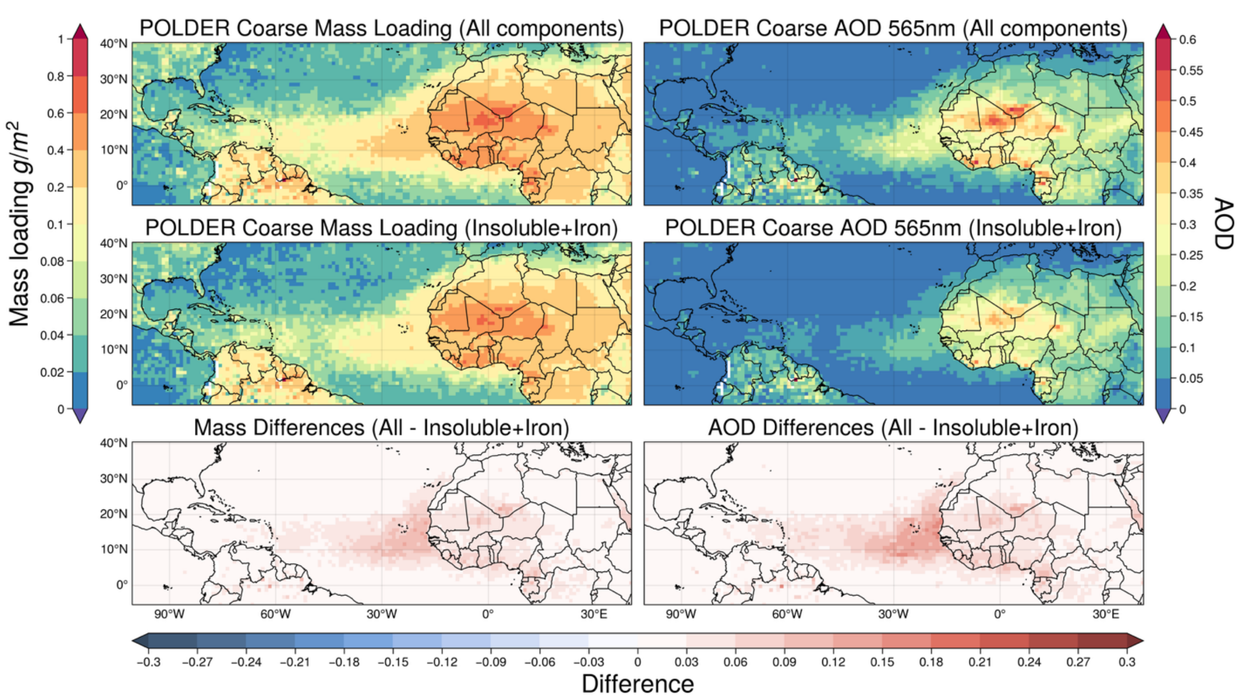

Figure S5: The POLDER coarse mass loading (left column) contributed by all aerosol components (left top), components of insoluble and iron (left middle), and the corresponding differences (left bottom). The POLDER coarse AOD at 565 nm (right column) contributed by all aerosol components (right top), components of insoluble and iron (right middle), and the corresponding differences (right bottom).

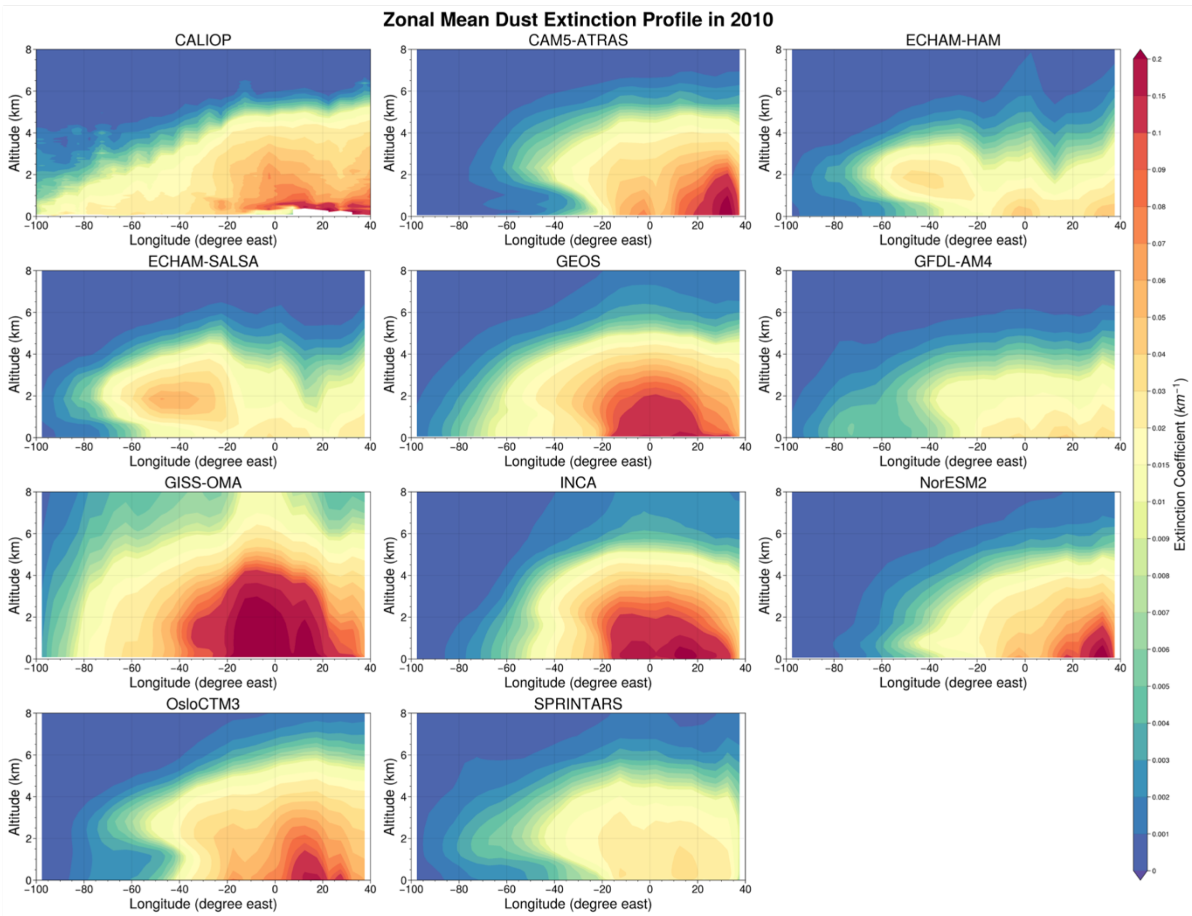

Figure S6: The vertical distribution of dust extinction coefficient (km^{-1}) from CALIOP and 10 AeroCom Phase III models (averaged over 5-25N).

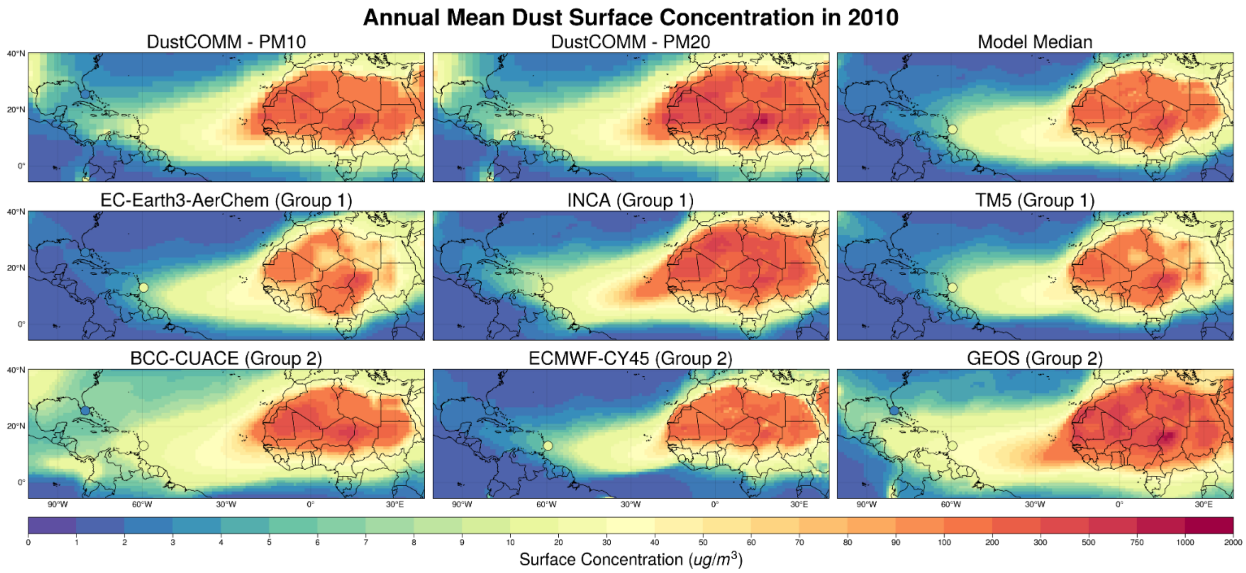

Figure S7: The dust surface concentration from 6 AeroCom Phase III models and the two in-situ measurements at Barbaos (13°6'N, 59°37'W) and Miami (25°45'N, 80°15'W) (colored dots).

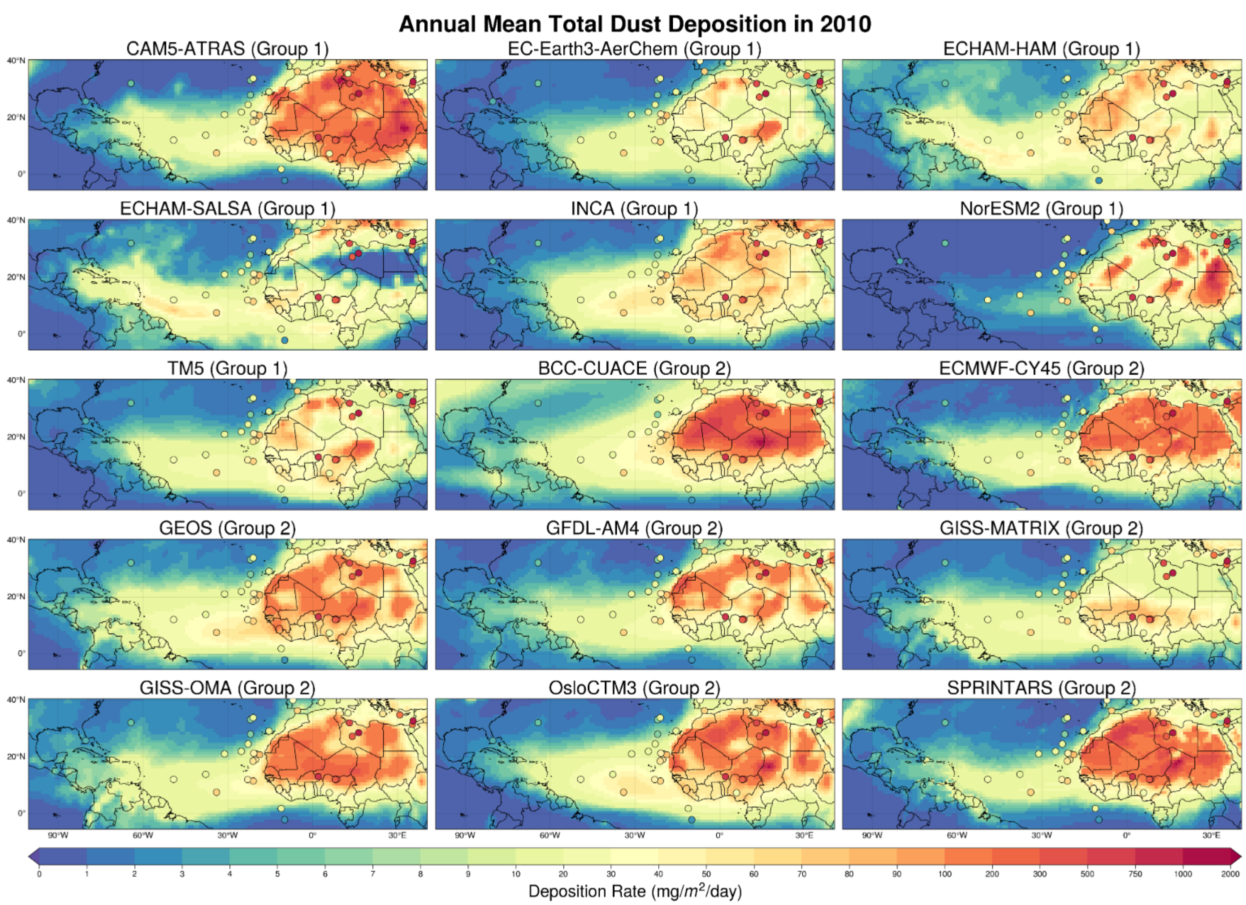

Figure S8: The dust total deposition distribution from 15 AeroCom Phase III models and the surface depotition observational data (colored dots).

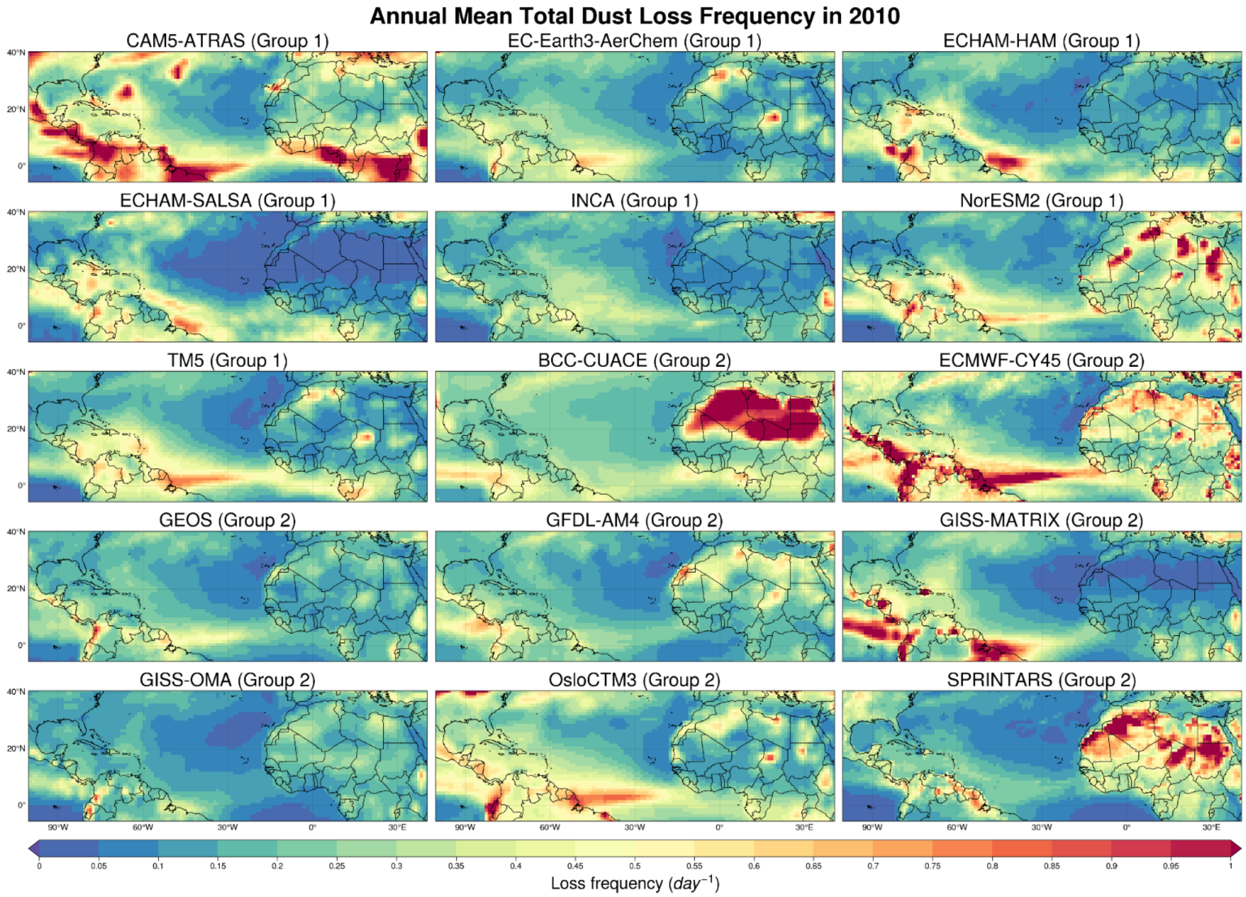

Figure S9: The dust loss frequency (d^{-1}) distribution from 15 AeroCom Phase III models.

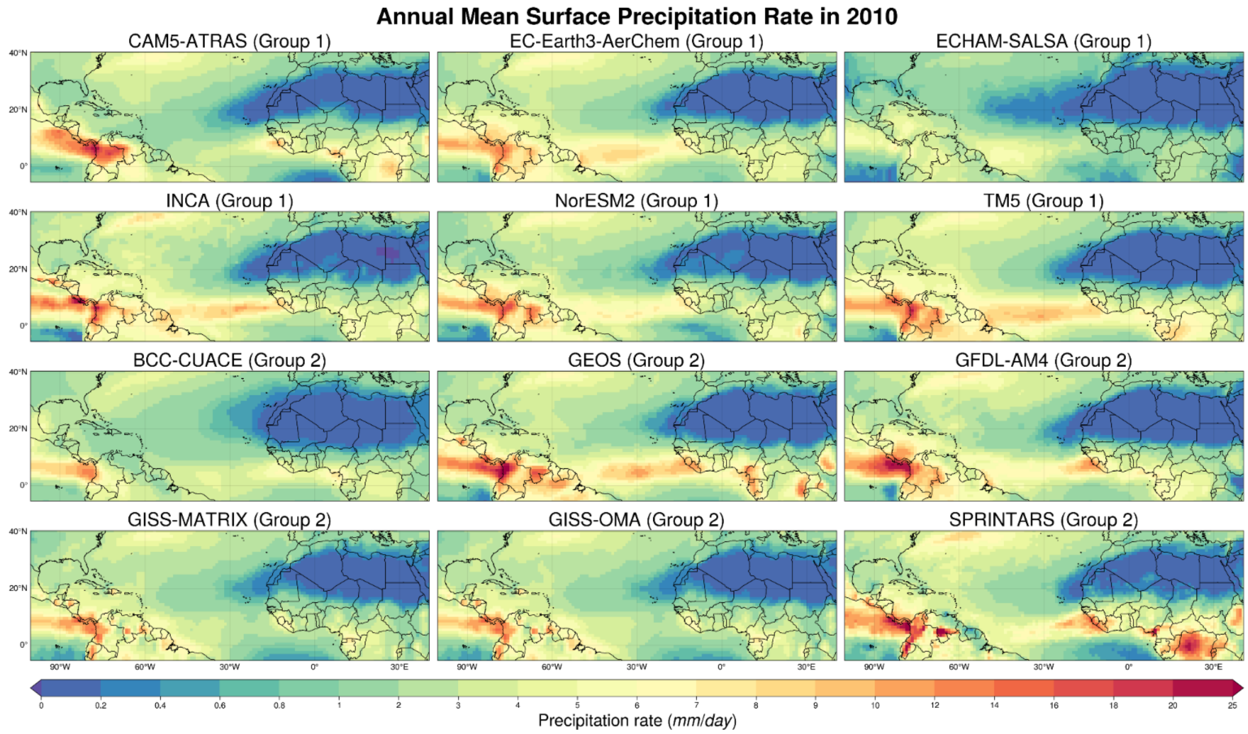

Figure S10: The surface precipitation rate (mm d^{-1}) from 12 AeroCom Phase III models.

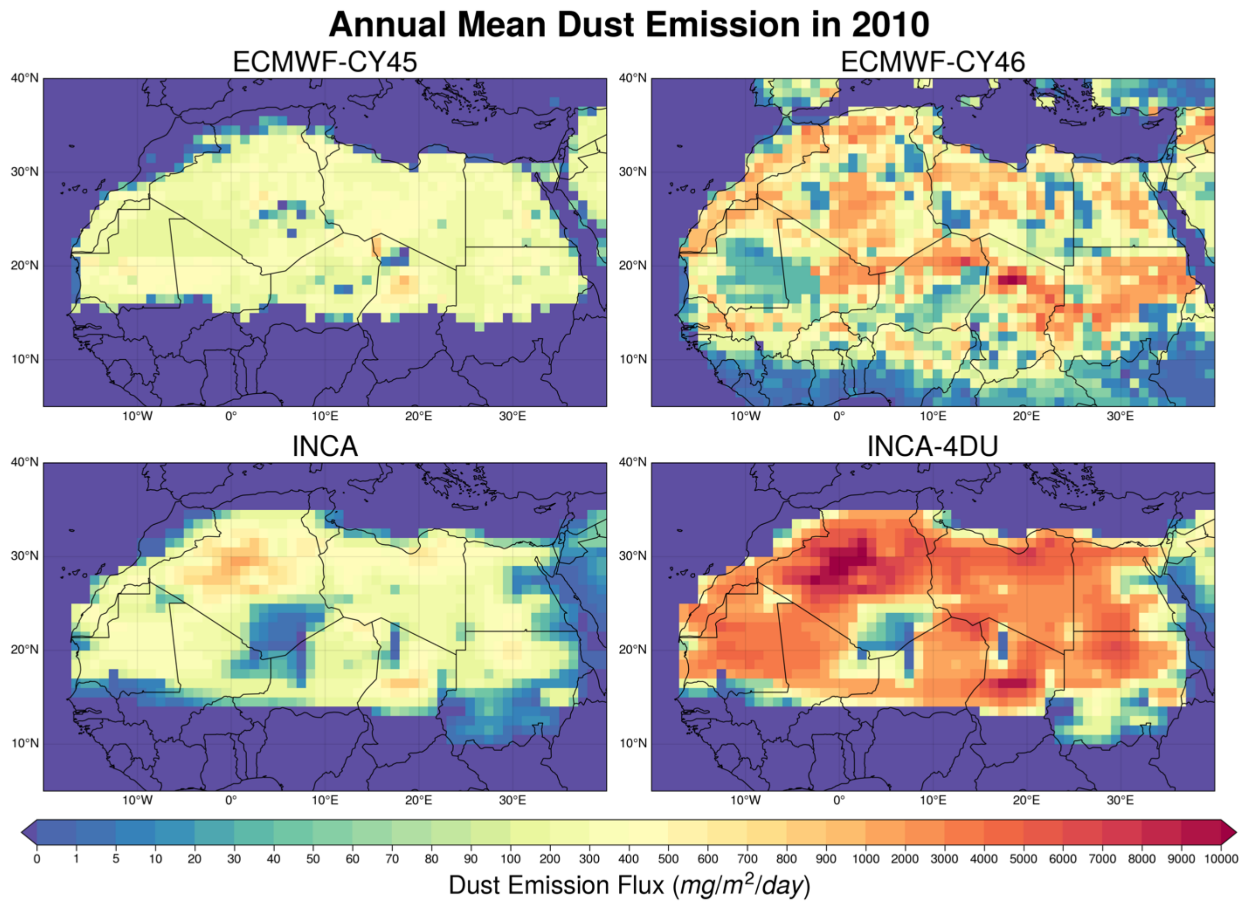

Figure S11: The dust emission of the four models.

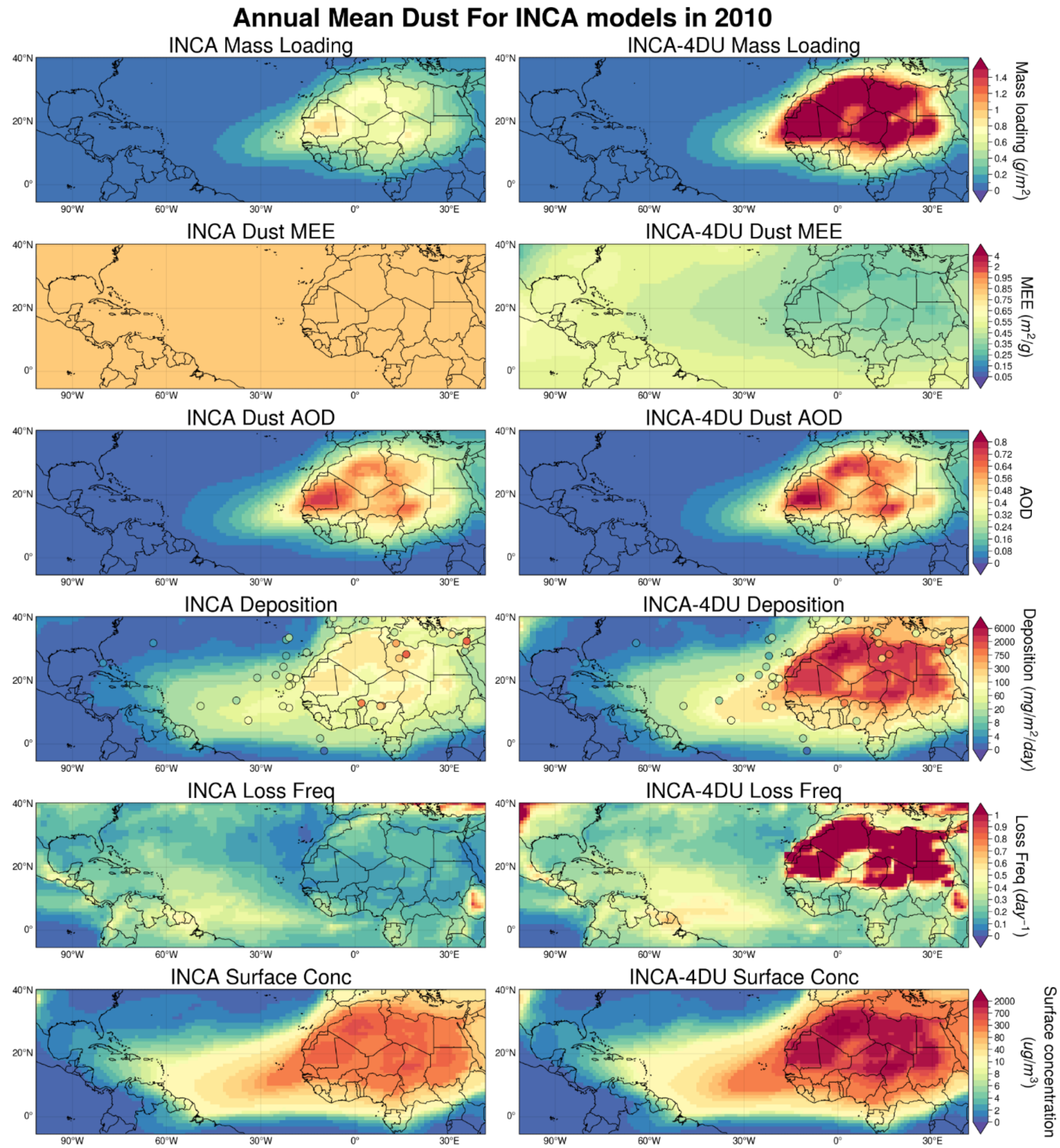

Figure S12: The dust AOD, MEE, mass loading, deposition, and loss frequency of the four models over the Trans-Atlantic.

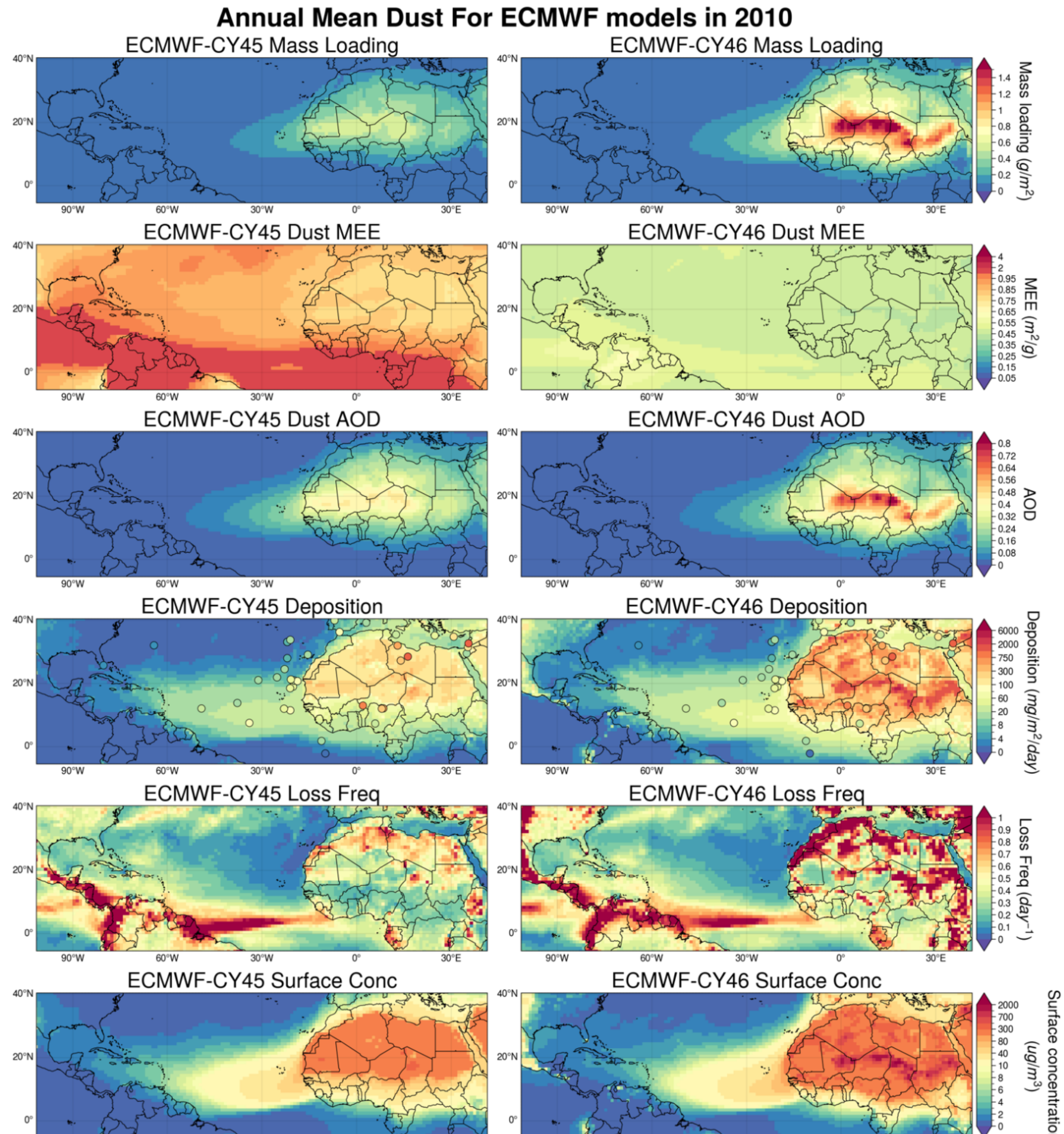

Figure S13: The dust AOD, MEE, mass loading, deposition, and loss frequency of the four models over the Trans-Atlantic.